



# Does the Lockstep Growth between Black Holes and Bulges Create Their Mass Relation?

Guang Yang (杨光)<sup>1,2,3,4</sup>, W. N. Brandt<sup>5,6,7</sup>, David M. Alexander<sup>8</sup>, Médéric Boquien<sup>9</sup>, Qingling Ni<sup>10</sup>, Casey Papovich<sup>1,2</sup>, Justin S. Spilker<sup>1,2</sup>, Fabio Vito<sup>11</sup>, Jonelle L. Walsh<sup>1,2</sup>, and Chengpeng Zhang<sup>1,2</sup>

<sup>1</sup> Department of Physics and Astronomy, Texas A&M University, College Station, TX 77843-4242, USA; [gyang206265@gmail.com](mailto:gyang206265@gmail.com)

<sup>2</sup> George P. and Cynthia Woods Mitchell Institute for Fundamental Physics and Astronomy, Texas A&M University, College Station, TX 77843-4242, USA

<sup>3</sup> Kapteyn Astronomical Institute, University of Groningen, P.O. Box 800, 9700 AV Groningen, The Netherlands

<sup>4</sup> SRON Netherlands Institute for Space Research, Postbus 800, 9700 AV Groningen, The Netherlands

<sup>5</sup> Department of Astronomy and Astrophysics, 525 Davey Lab, The Pennsylvania State University, University Park, PA 16802, USA

<sup>6</sup> Institute for Gravitation and the Cosmos, The Pennsylvania State University, University Park, PA 16802, USA

<sup>7</sup> Department of Physics, 104 Davey Laboratory, The Pennsylvania State University, University Park, PA 16802, USA

<sup>8</sup> Centre for Extragalactic Astronomy, Department of Physics, Durham University, South Road, Durham, DH1 3LE, UK

<sup>9</sup> Centro de Astronomía (CITEVA), Universidad de Antofagasta, Avenida Angamos 601, Antofagasta, Chile

<sup>10</sup> Institute for Astronomy, University of Edinburgh, Royal Observatory, Edinburgh, EH9 3HJ, UK

<sup>11</sup> Scuola Normale Superiore, Piazza dei Cavalieri 7, I-56126 Pisa, Italy

Received 2022 May 22; revised 2022 October 11; accepted 2022 October 17; published 2022 November 30

## Abstract

Recent studies have revealed a strong relation between the sample-averaged black hole (BH) accretion rate (BHAR) and star formation rate (SFR) among bulge-dominated galaxies—i.e., “lockstep” BH–bulge growth—in the distant universe. This relation might be closely connected to the BH–bulge mass correlation observed in the local universe. To further understand BH–bulge coevolution, we present Atacama Large Millimeter/submillimeter Array (ALMA) CO(2–1) or CO(3–2) observations of seven star-forming bulge-dominated galaxies at  $z = 0.5$ – $2.5$ . Using the ALMA data, we detect significant ( $>3\sigma$ ) CO emission from four objects. For our sample of seven galaxies, we measure (or constrain with upper limits) their CO line fluxes and estimate their molecular gas masses ( $M_{\text{gas}}$ ). We also estimate their stellar masses ( $M_{\text{star}}$ ) and SFRs, by modeling their spectral energy distributions. Using these physical properties, we derive the gas depletion timescales ( $\tau_{\text{dep}} \equiv M_{\text{gas}}/\text{SFR}$ ) and compare them with the bulge/BH growth timescales ( $\tau_{\text{grow}} \equiv M_{\text{star}}/\text{SFR} \sim M_{\text{BH}}/\text{BHAR}$ ). Our sample generally has  $\tau_{\text{dep}}$  shorter than  $\tau_{\text{grow}}$  by a median factor of  $\gtrsim 4$ , indicating that the cold gas will be depleted before significant bulge/BH growth takes place. This result suggests that BH–bulge lockstep growth is mainly responsible for maintaining the mass relation, not creating it. We note that our sample is small and limited to  $z < 2.5$ ; JWST and ALMA will be able to probe to higher redshifts in the near future.

*Unified Astronomy Thesaurus concepts:* Supermassive black holes (1663); Star formation (1569); Galaxy bulges (578); Molecular gas (1073); Spectral energy distribution (2129)

## 1. Introduction

From observations of the nearby universe, massive galaxies always host supermassive black holes (BHs) in their central regions, and the BH mass ( $M_{\text{BH}}$ ) is tightly correlated with the stellar mass ( $M_{\text{star}}$ ) of the host galaxy bulge (e.g., Kormendy & Ho 2013; Saglia et al. 2016). This tight BH–bulge mass correlation indicates that a physical connection between the BHs and the bulges exists in their cosmic evolution history. This connection is often called “BH–bulge coevolution.”

The specific coevolution mechanisms largely remain unknown. Some early studies proposed minor merger events as being the drivers of the tight BH–bulge mass relation in the local universe (e.g., Peng 2007; Jahnke & Macció 2011). The idea is based on the statistical central limit theorem: if low-mass galaxies are scattered around the  $M_{\text{BH}}$ – $M_{\text{star}}$  relation, the final system will be close to the mass relation, after many episodes of minor mergers. This scheme requires low-mass systems to be centered around the  $M_{\text{BH}}$ – $M_{\text{star}}$  relation. However, more recent observations have indicated that low-mass galaxies have  $M_{\text{BH}}$  systematically below the relation (e.g.,

Aird et al. 2018; Yang et al. 2018) and that some low-mass galaxies may not even host BHs (e.g., Greene et al. 2020). Therefore, minor mergers are unlikely to be the origin of the BH–bulge mass relation. Another idea about the origin of the  $M_{\text{BH}}$ – $M_{\text{star}}$  relation has to do with active galactic nucleus (AGN) feedback. A BH grows to a critical mass (related to  $M_{\text{bulge}}$ ) and launches a powerful wind that removes cold gas and/or prevents gas replenishment (e.g., King & Pounds 2015). The BH and stellar growth are thereby halted, due to the lack of fuel. This scenario requires strong negative AGN feedback on star formation (SF). However, this assumption still lacks strong observational support (e.g., Harrison 2017; Shangguan et al. 2020).

From an observational point of view, the  $M_{\text{BH}}$ – $M_{\text{star}}$  relation might result from connections between BH accretion and host galaxies. Previous observations on this topic have mostly focused on the connections between BH growth and the host galaxy  $M_{\text{star}}$  and the star formation rate (SFR) at different redshifts (see Section 3.3 of Brandt & Yang 2021 for a review). Some significant relations have been found. For example, BH growth strongly depends upon  $M_{\text{star}}$  at a given redshift (e.g., Georgakakis et al. 2017; Yang et al. 2017, 2018; Aird et al. 2018). However, it is not obvious how these relations are connected to the BH–bulge correlation in the local universe, mainly because these relations are for global galaxy (rather than bulge) properties. It is technically challenging to



Original content from this work may be used under the terms of the [Creative Commons Attribution 4.0 licence](https://creativecommons.org/licenses/by/4.0/). Any further distribution of this work must maintain attribution to the author(s) and the title of the work, journal citation and DOI.

investigate bulges, since galaxy angular sizes are generally small ( $\lesssim$  arcsec scales) in the distant universe ( $z \gtrsim 1$ ). Also, to avoid strong effects from the “morphological K correction” in the rest-frame UV, the sampled rest-frame wavelengths are required to be longer than  $\approx 4000\text{\AA}$  (e.g., Papovich et al. 2005; Conselice 2014). This means that the imaging should use IR bands ( $\gtrsim 1.2\text{ }\mu\text{m}$ ) to measure the morphologies of sources at  $z \approx 2$ , the cosmic epoch when AGN and SF activities peak. The Cosmic Assembly Near-infrared Deep Extragalactic Legacy Survey (CANDELS; Grogin et al. 2011; Koekemoer et al. 2011) provides high-angular resolution ( $\approx 0''.2$ ) and deep  $H$ -band imaging over a  $\approx 900\text{ arcmin}^2$  area, offering an excellent chance to study AGN–bulge connections at  $z \lesssim 3$ .

Using the CANDELS-based morphological measurements (Huertas-Company et al. 2015), as well as other multi-wavelength data, Yang et al. (2019) selected a sample of bulge-dominated galaxies and investigated their sample-averaged BH accretion rate (BHAR) versus SFR.<sup>12</sup> They found a significant linear correlation between BHAR and SFR for the bulge-dominated galaxies, and this correlation does not exist among their comparison sample, which features disks and/or irregularities (see, e.g., Kocevski et al. 2017; Ni et al. 2019, 2021 for related results). The best-fit BHAR/SFR ratio in Yang et al. (2019) is  $\approx 1/300$ , similar to the BH/bulge mass ratio observed in the local universe (e.g., Kormendy & Ho 2013). This “lockstep”-style growth between BHs and bulges can be useful for predicting BH accretion from bulge SF information. Based on a sample of bulge-dominated galaxies with well-measured SF histories (SFHs; Estrada-Carpenter et al. 2020), Yang et al. 2021 predicted BH accretion densities at high redshifts, which can be tested with JWST and future IR missions.

The BHAR–bulge SFR relation could be closely related to the BH–bulge mass relation in the local universe, given their similarities, as discussed above. However, a detailed picture of BH–bulge coevolution is still not clear, and there are two possible scenarios following the formation of the bulge:

1. The system initially retains a large amount of cold gas, which is available to fuel significant bulge growth. The BH would then continue to grow, following the BHAR–SFR relation. The galaxy would thereby move to  $M_{\text{BH}}/M_{\text{star}} \approx \text{BHAR}/\text{SFR} \approx 1/300$ , regardless of the previous ratio of  $M_{\text{BH}}/M_{\text{star}}$  in the pre-bulge phase. In this case, the BHAR–SFR relation plays the role of “creation” for the BH–bulge mass correlation.
2. The system initially has a limited or insignificant amount of cold gas remaining. The SF in the bulge will soon shut down, due to the lack of fuel, assuming that there is no further gas replenishment. The galaxy thereby remains in a low-specific SFR state and has a low BHAR (according to the BHAR–SFR relation), so it passively evolves. The  $M_{\text{BH}}/M_{\text{star}}$  “freezes” at the value in the pre-bulge phase. In this case, the BHAR–SFR relation plays the role of “maintenance” for the BH–bulge mass correlation.

Figure 1 illustrates the two scenarios above schematically. The determining factor between the two scenarios is the amount of

cold gas that is available after bulge formation. If the gas is abundant, then the more realistic scenario is the first one. The system has significant BH/bulge mass growth, reducing the scatter around the local  $M_{\text{BH}}\text{--}M_{\text{star}}$  relation (Figure 1, left). Otherwise, if the gas is limited, the system does not have much fuel to grow its BH/bulge mass, and its position on the  $M_{\text{BH}}\text{--}M_{\text{star}}$  diagram remains roughly the same. In this case, since the  $z=0$  position is near the  $M_{\text{BH}}\text{--}M_{\text{star}}$  relation, the current position should also be near the relation (Figure 1, right).

In this work, we assess the gas content of bulge-dominated galaxies using Atacama Large Millimeter/submillimeter Array (ALMA) observations. Our ALMA observations targeted CO(2–1) or CO(3–2) for seven bulge-dominated galaxies. For our targets, the low- $J$  transitions were the best possible lines accessible by ALMA to estimate  $M_{\text{gas}}$ , as they are not subject to strong assumptions about the CO spectral line energy distribution. Based on the ALMA data, we constrain the molecular gas content and discuss the implications for BH–bulge coevolution. We note that each of the seven individual systems should follow the BHAR–SFR relation (see Footnote 12), and thus they are suitable for testing the two scenarios laid out in Figure 1.

The structure of this paper is as follows. In Section 2, we reduce and analyze the ALMA data. We also compile existing multiwavelength data and perform a spectral energy distribution (SED) analysis. In Section 3, we discuss the physical implications of our results. We summarize our results and discuss future prospects in Section 4.

Throughout this paper, we assume a cosmology with  $H_0 = 70\text{ km s}^{-1}\text{ Mpc}^{-1}$ ,  $\Omega_M = 0.3$ , and  $\Omega_\Lambda = 0.7$ . We adopt a Chabrier initial mass function (IMF; Chabrier 2003). The quoted uncertainties are at the  $1\sigma$  (68%) confidence level. The word “gas” in this work specifically means cold molecular gas (mostly  $\text{H}_2$  and He), unless otherwise stated.

## 2. Data and Analysis

### 2.1. Targets and Observations

Our ALMA Cycle 7 program (2019.1.00678.S, PI: G. Yang) targeted seven bulge-dominated star-forming galaxies in the GOODS-South field, which has excellent multiwavelength coverage (see Section 2.5). The targets were selected from the bulge-dominated sample in Yang et al. (2019), and their basic properties are summarized in Table 1. The bulge-dominated sample is classified using machine-learning morphological measurements (Huertas-Company et al. 2015), based on Hubble Space Telescope (HST)  $H$ -band imaging (Grogin et al. 2011; Koekemoer et al. 2011). The machine-learning approach is efficient and reliable, and it has been successfully applied to other fields beyond GOODS-South (e.g., Huertas-Company et al. 2015; Ni et al. 2021). This targeting approach is designed to select pure spheroidal galaxies that do not have a disk component (see, e.g., Figure 2 of Yang et al. 2019), and we discuss the consequences of missing a disk component in Section 3.1. It is essential to focus on bulge-dominated galaxies, as the BHAR–SFR relation does not exist among other (e.g., disk or irregular) galaxies (Yang et al. 2019). Consistently, in the local universe, BH masses are only tightly correlated with the masses of bulges, rather than disks (e.g., Kormendy & Ho 2013).

<sup>12</sup> This sample-averaged BHAR is designed to overcome short-term ( $\lesssim 10^7\text{ yr}$ ) AGN variability effects and to approximate the long-term BH growth rate (e.g., Hickox et al. 2014). Therefore, individual bulge-dominated systems should follow the same BHAR–SFR relation over cosmic evolution timescales ( $\gtrsim 10^8\text{ yr}$ ).

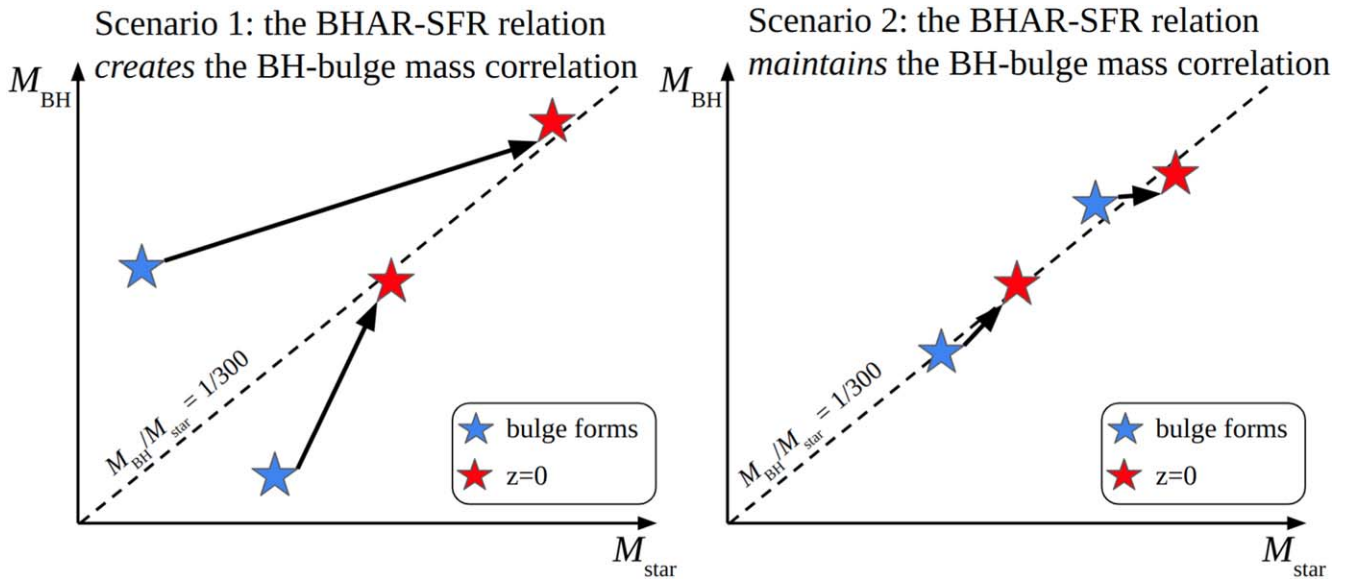


**Figure 1.** Schematic diagram of the two scenarios tested in this work. The blue and red stars represent the bulge formation redshift and  $z = 0$ , respectively. The black arrows indicate the evolution paths. The dashed line represents the observed BH–bulge mass relation in the local universe. The determining factor between the two scenarios is the amount of cold gas that is available after bulge formation (see Section 1 for details).

Our ALMA targets are selected to have secure optical spectroscopic redshift (spec- $z$ ) measurements from the literature, and the redshifts span  $z = 0.5$ – $2.5$  (see Table 1). The spec- $z$  measurements are necessary to locate the observed frame CO frequencies and target them with ALMA. The sample is also selected to have Spitzer/MIPS and/or Herschel (signal-to-noise ratio or  $S/N > 3$ ) detections (Section 2.5), so that they are likely at the early star-forming phase after bulge formation (Section 1). The Herschel flux uncertainties are based on Monte Carlo simulations that account for both instrument and confusion noise (Elbaz et al. 2011). We are primarily interested in star-forming rather than quiescent bulges. This is because for quiescent systems, both the bulge and the BH growth have essentially ceased, according to the BHAR–bulge SFR relation (Yang et al. 2019), and the system is already in place on the  $M_{\text{BH}}$ – $M_{\text{star}}$  relation.<sup>13</sup> Five (out of seven) targets are classified as X-ray AGNs in Luo et al. (2017). This prevalence of AGNs is naturally expected from the BHAR–bulge SFR relation, as our targets are selected to be star-forming bulge-dominated galaxies.

The ALMA data were taken on 2020 January 14 and 24, with the on-site perceptible water vapor, ranging from 4.6 to 6.6 mm. We target CO(2–1) and CO(3–2) for  $z < 2$  and  $z > 2$  sources in our sample, respectively. These lines are within the frequency ranges covered ALMA bands 3 and 4. Among the four spectral windows (SPWs), one SPW was centered on the line, and the other three covered continuum frequencies. These observations were performed on a 12 m array configuration of C-3 (maximum baseline = 0.5 km), resulting in angular resolutions of  $1''.1$ – $2''.3$ . The on-source exposure time was 24–28 minutes, reaching a  $1\sigma$  continuum sensitivity of  $\approx 0.02$ – $0.03$  mJy beam $^{-1}$ .

<sup>13</sup> The program actually observed 10 targets in total. These 10 targets were originally selected using an earlier IR catalog, PACS Evolutionary Probe (PEP; Lutz et al. 2011). However, the most recent catalog (Barro et al. 2019; Section 2.5), which carefully addresses the question of source confusion, indicates that three targets are actually quiescent, being undetected in the IR. Therefore, we only focus on the remainder of the targets, i.e., seven IR star-forming galaxies.

## 2.2. Data Reduction

We requested and downloaded the calibrated Measurement Sets (MSs) for our observations, using the online Science Ready Data Products service.<sup>14</sup> These MS data are produced by the ALMA Pipeline v6.1.2–7. We use the Common Astronomy Software Applications (CASA) v6.2 package to further reduce these MS data.

We employ the “tclean” function in CASA to produce the primary beam–corrected continuum images from the visibility data. We include all available SPWs (masking potential line channels within  $\pm 500$  km s $^{-1}$  around the line center). We set the output image size to  $20'' \times 20''$ , with a pixel scale of  $0''.2$ . We then apply the “imfit” function (CASA) to these images to determine the source continuum position. Five sources have converged fits, but none of them are significant ( $S/N > 3$ ), indicating that the continuum emission is weak. We present a quantitative analysis of the continuum fluxes in Section 2.4.

For the line analysis, we first utilize tclean to transform the visibility data into an image cube for each source. We use the line SPW and set the output spectral channel width to 50 km s $^{-1}$  (data set native resolution  $\approx 1$ – $3$  km s $^{-1}$ ), while the spaxel size and pixel scale are the same as above. Using “imcollapse” (CASA), we then collapse the cube along the frequency axis, including the line frequency (inferred from the optical redshift)  $\pm 300$  km s $^{-1}$ . Based on the resulting line image, we perform source detection with “imfit” (CASA), which searches for a Gaussian-shaped source. If a source is detected with  $S/N > 3$ , we adopt the imfit source position for spectrum extraction below; otherwise, we adopt the CANDELS position (Table 1).

The empirical choice of collapsing the data cube within  $\pm 300$  km s $^{-1}$  is to cover most of the line signal, as the CO line width is typically  $\lesssim 600$  km s $^{-1}$  in the literature (e.g., Freundlich et al. 2019; Shangguan et al. 2020). Choosing an even larger width could dilute the  $S/N$ . We also test different ranges other than  $\pm 300$  km s $^{-1}$  (see Section 2.3) and find

<sup>14</sup> <https://data.nrao.edu/portal/#/>



**Table 1**  
Basic Source Properties

ID (1)	R.A. (2)	Decl. (3)	$z$ (4)	$z$ References (5)	$\log M_{\text{star}}$ (6)	$\log \text{SFR}$ (7)	$\log L_X$ (8)	$\tau_{\text{grow}}$ (9)	$t_{\text{ua}}$ (10)
528	53.113468	−27.933294	1.089	Cooper et al. (2012)	$11.28 \pm 0.10$	$1.58 \pm 0.04$	$41.75 \pm 0.16$	$5.09 \pm 1.25$	5.42
6278	53.060116	−27.852997	1.540	Suh et al. (2015)	$10.97 \pm 0.05$	$1.42 \pm 0.23$	$43.00 \pm 0.07$	$3.52 \pm 1.88$	4.11
23845	53.097649	−27.715282	2.142	Coil et al. (2015)	$10.96 \pm 0.02$	$2.05 \pm 0.02$	$43.41 \pm 0.09$	$0.80 \pm 0.06$	3.02
24210	53.071419	−27.717581	0.566	Cooper et al. (2012)	$10.58 \pm 0.05$	$1.89 \pm 0.02$	$42.87 \pm 0.05$	$0.49 \pm 0.06$	7.98
24682	53.104096	−27.683758	0.732	Cooper et al. (2012)	$10.78 \pm 0.02$	$0.58 \pm 0.04$	$42.98 \pm 0.05$	$15.73 \pm 1.62$	6.99
25573	53.139187	−27.694145	1.044	Vanzella et al. (2008)	$11.00 \pm 0.02$	$1.14 \pm 0.04$	—	$7.23 \pm 0.76$	5.58
25998	53.137573	−27.700104	2.453	Barro et al. (2013)	$11.05 \pm 0.07$	$2.33 \pm 0.06$	$43.68 \pm 0.08$	$0.53 \pm 0.11$	2.63

**Note.** Column (1): identification in the CANDELS catalog (Guo et al. 2013). Columns (2) and (3): CANDELS J2000 coordinates. Column (4): optical spectroscopic redshift. Column (5): redshift reference. Columns (6) and (7): logarithmic stellar mass ( $M_{\odot}$ ) and SFR ( $M_{\odot} \text{ yr}^{-1}$ ) from our SED modeling (see Section 2.5). Column (8): intrinsic X-ray luminosity ( $\text{erg s}^{-1}$ ), based on the absorption-corrected X-ray flux (see Section 2.5); “—” means X-ray not detected; we note that  $L_X$  only reflects instantaneous AGN activity, not long-term average BH growth (see Section 1). Column (9): the bulge stellar growth timescale (Gyr), as defined in Equation (5). Column (10): the universe’s age (Gyr) at the source’s redshift.

similar results. Admittedly, if a line center has a large shift, greater than  $300 \text{ km s}^{-1}$ , our method could miss it. However, from our extracted spectra, we do not find such strong shifts (see Section 2.3).

### 2.3. Line Flux Measurements

We extract the CO spectrum for each source with CASA’s “specflux,” utilizing a circular aperture with an area of two times the beam area. Here, we choose a fixed aperture, instead of an adaptive aperture based on, e.g., contours. This is because our targets are generally faint and significantly affected by random noise. The latter adaptive approach, which favors “positive” and avoids “negative” noise, may potentially introduce a positive bias. This bias could lead to S/N overestimation and even false detections. The resulting spectra are displayed in Figure 2. From these spectra, there do not appear to be any significant line signals beyond  $300 \text{ km s}^{-1}$ , supporting our source detection method in Section 2.2.

We then fit the CO spectrum for each source with CASA’s “specfit,” employing a Gaussian model. Here, we do not include a continuum component, because the continua are insignificant for all of our sources (see Section 2.4). To avoid false detections, we require the Gaussian center ( $v_{\text{cent}}$ ) to be within  $\pm 200 \text{ km s}^{-1}$ , where the velocity zeropoint corresponds to the line frequency inferred from the optical redshift (and hereafter). The fits converge for six (of seven) sources. We obtain their best-fit  $v_{\text{cent}}$  and FWHM from the specfit results. For each of the six sources, we estimate the velocity-integrated line flux (units:  $\text{Jy km s}^{-1}$ ) by integrating the CO spectra over the range of ( $v_{\text{cent}} - \text{FWHM}$ ,  $v_{\text{cent}} + \text{FWHM}$ ). For the other source (CANDELS 23845), we perform the integral over ( $-300 \text{ km s}^{-1}$ ,  $+300 \text{ km s}^{-1}$ ).

To estimate the line flux uncertainty for each source, we randomly place  $\approx 20$  nonoverlapping apertures around each source (avoiding the spectrum extraction region). For each aperture, we then extract the spectrum and measure the velocity-integrated flux in the same way as above. We calculate the standard deviations of these fluxes. We repeat this process 100 times, obtaining 100 standard deviation values, then calculate the median of these values. Finally, we adopt the median as the CO flux  $1\sigma$  uncertainty for each source. If a source has a CO flux  $\text{S/N} > 3$ , we consider the line to be detected, and four of seven sources have CO detected. For the

other three sources, we adopt three times the CO flux errors as their upper limits. In Section 2.2, we collapse the data cubes over  $\pm 300 \text{ km s}^{-1}$  for an initial source search. We also test collapsing at other velocity ranges, from  $\pm 100 \text{ km s}^{-1}$  to  $\pm 500 \text{ km s}^{-1}$ , but do not find additional CO detections beyond the four sources. Therefore, we conclude that our results are not sensitive to the collapsed velocity range.

Since the line flux above is measured within an aperture (hereafter, “aperture flux”), we need to conduct an aperture correction to account for the emission outside the aperture. To perform this task, we use a large circular aperture, with an area of four times the beam area, to estimate the “total” line flux for our highest-S/N source (CANDELS 528, with  $\text{S/N} \approx 8$ ). We then divide this total flux by the aperture flux and adopt the result as our aperture correction factor ( $= 1.12$ ). We multiply the line flux/error (or upper limit) by this aperture correction factor. We also test estimations of the correction factor, based on the three other detected sources. The resulting corrections are 1.10–1.28, similar to our adopted value (1.12). Our adopted correction is based on the highest-S/N source, and thus it should be the most reliable. We note that our main results (Section 3) are not sensitive to the choice of the aperture correction factor, as all the values (from 1.10 to 1.28) are relatively small.

Table 2 lists the final CO fluxes, errors, and upper limits for our sources. For the four CO-detected sources, we present spatial analyses of their CO emission in the Appendix. In brief, the angular resolutions of our ALMA observations are not sufficient to well resolve the detected CO emission.

From the measurements of the CO line fluxes above, we estimate the CO luminosities following Solomon & Vanden Bout (2005), i.e.:

$$L'_{\text{CO}}(J, J-1) = 3.25 \times 10^7 I_{\text{CO}} \nu_{\text{obs}}^{-2} D_L^2 (1+z)^{-3}, \quad (1)$$

where  $I_{\text{CO}}$  is the velocity-integrated line velocity in  $\text{Jy km s}^{-1}$ ;  $\nu_{\text{obs}}$  is the line frequency in the observed frame;  $D_L$  is the luminosity distance in Mpc; and  $L'_{\text{CO}}(J, J-1)$  is in units of  $\text{K km s}^{-1} \text{ pc}^2$ . Assuming  $r_{21} = L'_{\text{CO}}(2, 1)/L'_{\text{CO}}(1, 0) = 0.8$  and  $r_{31} = L'_{\text{CO}}(3, 2)/L'_{\text{CO}}(1, 0) = 0.5$  (e.g., Saintonge et al. 2017; Lamperti et al. 2020), we can convert the observed  $L'_{\text{CO}}(J, J-1)$  ( $J=3$  or  $2$ ) to  $L'_{\text{CO}}(1, 0)$  (hereafter,  $L'_{\text{CO}}$ ). Finally, we estimate the molecular mass from

$$M_{\text{gas}} = \alpha_{\text{CO}} L'_{\text{CO}}, \quad (2)$$

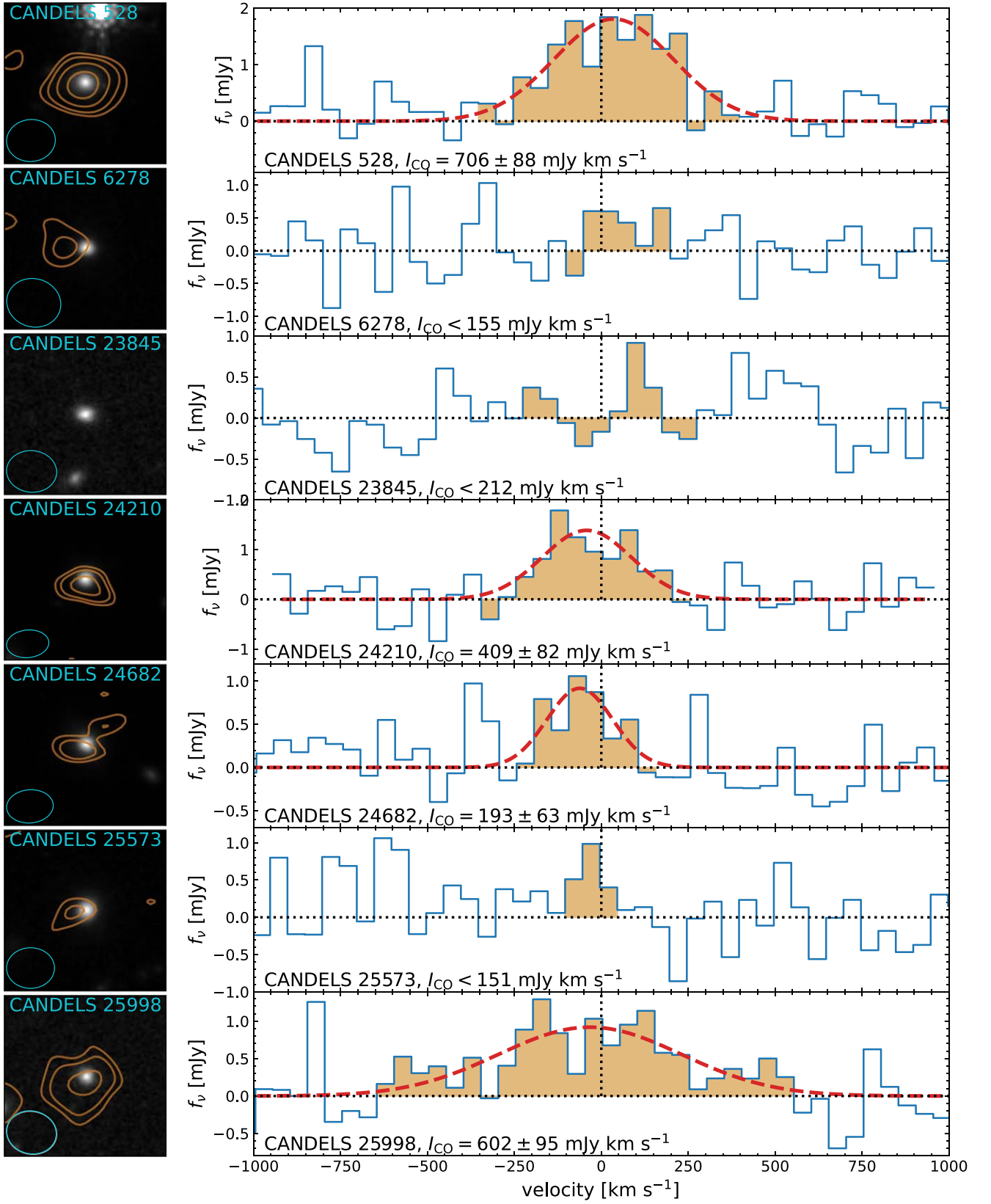


**Figure 2.** Left: HST *H*-band 7'' × 7'' cutouts, with contours of CO emission. The contours are at the 2 $\sigma$ , 3 $\sigma$ , 5 $\sigma$ , and 8 $\sigma$  levels. The beam profile is displayed in the bottom left corner. There is no contour for CANDELS 23845, due to the weak signal of its CO line map. Right: CO spectrum for each source. The red dashed curve represents the best-fit Gaussian model (only displayed for CO-detected sources). The horizontal and vertical dotted lines indicate zero flux and velocity, respectively. The orange shaded region indicates the integrated velocity range for the line flux measurement. The measured line flux and its uncertainty (or upper limit) is labeled. We consider the line to be detected if  $S/N > 3$ ; we adopt the 3 $\sigma$  uncertainties as upper limits for undetected sources (see Table 2).

**Table 2**  
ALMA Results

ID (1)	$J$ (2)	Amp. (3)	$v_{\text{cent}}$ (4)	$\Delta v$ (5)	$L_{\text{CO}}$ (6)	$\log M_{\text{gas}}$ (7)	$\tau_{\text{dep}}$ (8)	$\mu$ (9)	$S_{\nu}^{\text{cont}}$ (10)	$\log M_{\text{gas}}^{\text{cont}}$ (11)
528	2	$1.81 \pm 0.22$	$35 \pm 24$	$404 \pm 56$	$706 \pm 88$	$10.78 \pm 0.05$	$1.58 \pm 0.24$	$0.31 \pm 0.08$	$<79$	$<10.75$
6278	2	...	...	...	$<155$	$<10.41$	$<0.96$	$<0.27$	$<70$	$<10.98$
23845	3	...	...	...	$<212$	$<10.65$	$<0.40$	$<0.49$	$<80$	$<10.95$
24210	2	$1.39 \pm 0.24$	$-42 \pm 26$	$303 \pm 62$	$409 \pm 82$	$9.97 \pm 0.09$	$0.12 \pm 0.02$	$0.24 \pm 0.06$	$<93$	$<10.25$
24682	2	$0.92 \pm 0.24$	$-62 \pm 28$	$223 \pm 67$	$193 \pm 63$	$9.87 \pm 0.14$	$1.93 \pm 0.65$	$0.12 \pm 0.04$	$<95$	$<10.49$
25573	2	...	...	...	$<151$	$<10.07$	$<0.86$	$<0.12$	$<77$	$<10.70$
25998	3	$0.92 \pm 0.15$	$-33 \pm 51$	$618 \pm 119$	$602 \pm 95$	$11.21 \pm 0.07$	$0.76 \pm 0.16$	$1.43 \pm 0.32$	$<88$	$<11.10$

**Note.** Column (1): identification in the CANDELS catalog. Column (2): targeted CO transition ( $J \rightarrow J - 1$ ). Columns (3), (4), and (5): Gaussian amplitude (mJy), central velocity ( $\text{km s}^{-1}$ ; relative to that from the optical redshift), and FWHM ( $\text{km s}^{-1}$ ), from the fit of the CO spectrum; “-” indicates CO not detected ( $S/N < 3$ ). Column (6): velocity-integrated CO flux or  $3\sigma$  upper limit (if  $S/N < 3$ ), in  $\text{mJy km s}^{-1}$ . Columns (7), (8), and (9): logarithmic gas mass ( $M_{\odot}$ ) or  $3\sigma$  upper limit (inferred from  $L'_{\text{CO}}$ ; see Section 2.3), gas depletion timescale (Gyr), and gas-to-stellar mass ratio. Columns (10) and (11):  $3\sigma$  upper limit of the continuum flux ( $\mu\text{Jy}$ ) and corresponding logarithmic gas mass ( $M_{\odot}$ ).

where we assume the conversion factor  $\alpha_{\text{CO}} = 4.3 M_{\odot} (\text{K km s}^{-1} \text{pc}^2)^{-1}$  (hereafter, we use these units for  $\alpha_{\text{CO}}$ ), a typical value that is adopted in the literature (e.g., Bolatto et al. 2013; Carilli & Walter 2013). This adopted conversion factor includes the contribution from helium and metals. We discuss the effects of this  $\alpha_{\text{CO}}$  assumption in Section 3.1. Table 2 lists the resulting  $L'_{\text{CO}}$  and  $M_{\text{gas}}$ .

#### 2.4. Continuum Emission

In Section 2.2, we performed a source search on the ALMA continuum images, but did not find any significant detections. Therefore, we adopt the CO line position (if available) or the CANDELS position for the continuum measurements. As for the line flux extraction, we also employ a circular aperture, with area =  $2 \times$  the beam area, to measure the continuum flux. We estimate the noise by randomly placing apertures and calculating the standard deviations of the resulting continuum fluxes (a similar procedure as in Section 2.3). None of our sources have  $S/N > 3$  continuum fluxes, consistent with the results in Section 2.2. As in Section 2.3, we also adopt three times the noise as the continuum upper limit for each source (listed in Table 2). We then convert these flux upper limits into  $L_{\nu, 850 \mu\text{m}}$  (rest-frame  $850 \mu\text{m}$  luminosity) upper limits, assuming the Rayleigh–Jeans law ( $L_{\nu} \propto \nu^2$ ) for  $K$  corrections. Finally, we constrain the continuum-based gas masses using the scaling relation— $M_{\text{gas}}^{\text{cont}} = L_{\nu, 850 \mu\text{m}} / (1.01 \times 10^{20} \text{ erg s}^{-1} \text{ Hz}^{-1} M_{\odot}^{-1})$ —from Scoville et al. (2016, 2017).<sup>15</sup>

The resulting  $M_{\text{gas}}^{\text{cont}}$  upper limits are listed in Table 2. For three of the four CO-detected sources (except CANDELS 25998), the CO-based masses are consistent with the continuum-based constraints. For CANDELS 25998, the CO-based mass is slightly higher than the continuum-based upper limit, by  $\approx 0.1$  dex (see Section 3.1 for more discussion of this object). For the three CO-undetected sources, the CO-based mass constraints are tighter than the continuum-based ones. Therefore, our scientific discussions are primarily based on the CO measurements in Section 3, unless otherwise stated.

#### 2.5. Multiwavelength SEDs

We employ CIGALE v2022.0 (Roehlly et al. 2014; Boquien et al. 2019; Yang et al. 2020, 2022) to perform SED modeling for our ALMA sources. We compile multiwavelength broadband photometric data from the Rainbow Cosmological Surveys Database.<sup>16</sup> These data include 23 bands from  $U$  to SPIRE  $500 \mu\text{m}$  (Guo et al. 2013; Barro et al. 2019). We also compile X-ray photometry from the 7 Ms Chandra Deep Field-South catalog (Luo et al. 2017). Six sources (all except CANDELS 25573) have X-ray detections. Among them, five are detected in the hard band (2–7 keV), and we adopt their hard-band fluxes, which are less affected by obscuration compared to the full-band (0.5–7 keV) and soft-band (0.5–2 keV) fluxes. Since CIGALE requires obscuration-corrected X-ray fluxes as inputs (Yang et al. 2020, 2022), we apply obscuration corrections to these adopted fluxes. The corrections are estimated based on the absorption column densities ( $N_{\text{H}}$ ) from Luo et al. (2017) and PIMMS.<sup>17</sup> One source (CANDELS 528) is only detected in the soft band, and we adopt the soft-band flux.<sup>18</sup>

The model parameters in CIGALE are listed in Table 3. We adopt a delayed- $\tau$  model (sfhdelayed in CIGALE) for the SFH, and a Bruzual & Charlot 2003 model (bc03 in CIGALE) for a simple stellar population (SSP). We note that when fitting the data, CIGALE automatically excludes unphysical models in which the stellar age is older than the universe’s age. In bc03, we assume a Chabrier (2003) IMF and a solar metallicity ( $Z = 0.02$ ). We also include nebular emission (nebular in CIGALE), with default settings. We adopt the Charlot & Fall (2000) model (dustatt\_modified\_CF00 in CIGALE) for stellar attenuation. We allow the V-band attenuation to vary from 0.2 to 3 mag, while leaving the other parameters ( $\mu_V$ ,  $n_{\text{ISM}}$ , and  $n_{\text{BC}}$ ) at the default values. We use the Dale et al. (2014) model (dale2014 in CIGALE) for galactic dust emission. We allow three values for the radiation field slope, i.e., 1.5, 2, and 2.5. We use the SKIRTOR model (Stalevski et al. 2012, 2016; skirtor2016 in CIGALE) for the AGN UV-to-IR emission. We allow frac<sub>AGN</sub> (the fractional AGN IR

<sup>15</sup> The original scaling factor was  $6.7 \times 10^{19} \text{ erg s}^{-1} \text{ Hz}^{-1} M_{\odot}^{-1}$ , assuming  $\alpha_{\text{CO}} = 6.5$  (Scoville et al. 2016). Here, we modify the scaling factor so that the relation becomes consistent with our assumed  $\alpha_{\text{CO}} = 4.3$  (Section 2.3).

<sup>16</sup> [http://arcoirix.cab.inta-csic.es//Rainbow\\_navigator\\_public/](http://arcoirix.cab.inta-csic.es//Rainbow_navigator_public/)

<sup>17</sup> <https://cxc.harvard.edu/toolkit/pimms.jsp>

<sup>18</sup> Obscuration correction is not possible for this source, due to the single-band detection. However, we do not expect the obscuration to be strong, because otherwise the detected band would likely be the hard band, rather than the soft band.

**Table 3**  
CIGALE Model Parameters

Module	Parameter	Symbol	Values
SFH	Stellar e-folding time	$\tau_{\text{star}}$	0.5, 1, 2, 3, 4, 5 Gyr
sfhdelayed	Stellar age	$t_{\text{star}}$	0.2, 0.5, 1, 2, 3, 4, 5 Gyr
SSP	IMF	...	Chabrier (2003)
bc03	Metallicity	$Z$	0.02
Dust attenuation	V-band attenuation in the ISM	$A_V^{\text{ISM}}$	0.2–1 (step 0.1), 1.5, 2, 2.5, 3 mag
dustatt_modified_CF00	$A_V^{\text{ISM}} / (A_V^{\text{ISM}} + A_V^{\text{BC}})$	$\mu_V$	0.44
	Slope of the ISM attenuation	$n_{\text{ISM}}$	−0.7
	Slope of the birth cloud attenuation	$n_{\text{BC}}$	−1.3
Galactic dust emission	Slope in $dM_{\text{dust}} \propto U^{-\alpha_{\text{dust}}} dU$	$\alpha_{\text{dust}}$	1.5, 2, 2.5
dale2014	Ratio of $L_{\text{mbb}}$ and $L_{\text{dale2014}}$	$\epsilon_{\text{mbb}}$	0, 1, 2, 5, 10, 20, 50
mbb <sup>a</sup>	Temperature of mbb	$T_{\text{mbb}}$	50, 100 K
	Emissivity of mbb	$\beta$	1.5
AGN (UV-to-IR) emission	AGN contribution to IR luminosity	$\text{frac}_{\text{AGN}}$	0–0.9 (step 0.1), 0.99
skirtor2016	Viewing angle	$\theta_{\text{AGN}}$	30°, 70°
	Polar dust color excess	$E(B - V)_{\text{PD}}$	0.03, 0.2, 0.4
X-ray emission	Maximum deviation from the $\alpha_{\text{ox}} - L_{\nu, 2500\text{\AA}}$ relation	$ \Delta\alpha_{\text{ox}} _{\text{max}}$	0.2
xray	AGN X-ray angle coefficients	$(a_1, a_2)$	(0.5, 0)

**Note.** For the parameters not listed here, we use the default values. (a) The mbb module is only used for CANDELS 23845, 24210, and 25998, to improve their fit quality (see Section 2.5).

luminosity) to vary between 0 and 0.99. We set  $\theta_{\text{AGN}}$  (the viewing angles) to 30° and 70°, which are typical values for type 1 and type 2 AGNs, respectively (e.g., Yang et al. 2020; Ramos Padilla et al. 2022). Finally, we include the xray module in CIGALE, to account for AGN/galaxy X-ray emission, and leave the related parameters at the default value(s). The CIGALE configurations above lead to a total of 27,243,160 models (3,891,880 per source). In addition to the photometry above, we also include the ALMA continuum upper limits (Section 2.4) in the fits.

We run CIGALE with the configurations above. For four of seven sources, the fit quality is acceptable, with reduced  $\chi^2 < 2$  (see Figure 3 for the best-fitting SEDs). We adopt the Bayesian output of  $M_{\text{star}}$  and SFR (Table 1).<sup>19</sup> However, for CANDELS 23845, 24210, and 25998, the observed far-IR fluxes are systematically higher than the model values, leading to a large reduced  $\chi^2 \approx 4$ –5. This “far-IR excess” might be caused by a dust-enshrouded stellar population that is strongly attenuated at shorter wavelengths (e.g., Hodge et al. 2016; Buat et al. 2019). We note that CANDELS 23845, 24210, and 25998 are actually similar to the sample of Buat et al. (2019); i.e., they are all massive ( $\log(M_{\text{star}}/M_{\odot}) \gtrsim 10.5$ ) dust-rich ( $\log(L_{\text{IR}}/L_{\odot}) \gtrsim 12$ ) galaxies. The Buat et al. (2019) sample’s continuum emission is detected by ALMA, but ours is not (Section 2.4). We consider this difference to be due to the different ALMA bands being used (band 6 versus band 3), with the dust emission being stronger at shorter ALMA wavelengths, due to the Rayleigh–Jeans law (e.g., Figure 2 of Scoville et al. 2016).

For these three sources, we include an additional ad hoc modified (flexible emissivity) blackbody model (mbb in CIGALE) to account for this far-IR excess (Table 3), and rerun

CIGALE. This mbb component is designed to model the far-IR emission from the dust-enshrouded stellar population, as discussed above. To account for the possible temperature variance of this hidden population, we allow a cold model (50 K) and a hot model (100 K) in the mbb (see Table 3). We allow the luminosity ratio,  $L_{\text{mbb}}/L_{\text{dale2014}}$ , varying from 0 to 50.

Indeed, the new fits have improved fit quality (reduced  $\chi^2 \approx 1$ –2; see Figure 3) compared to the previous fits. After adding the new component, the Akaike information criterion (Akaike 1974) is reduced by  $>10$ , indicating that the improvements with mbb are statistically significant (e.g., Burnham & Anderson 2002).

For the new fits, we do not adopt the SFRs directly from the CIGALE output, because the CIGALE SFRs do not account for the mbb contribution that dominates the galaxy IR luminosity ( $L_{\text{IR, gal}}$ ). We estimate the SFRs based on the fitted total galaxy IR luminosity, excluding the AGN contribution (Kennicutt 1998; Salim et al. 2007), i.e.,

$$\text{SFR} = 1.09 \times 10^{-10} L_{\text{IR, gal}}, \quad (3)$$

where SFR and  $L_{\text{IR, gal}}$  are both in solar units. We still adopt the output  $M_{\text{star}}$ , assuming that the stellar mass is dominated by the main stellar population, rather than the hidden population. This assumption is justifiable, because the near-IR data (rest frame  $\sim 1 \mu\text{m}$ ), a robust  $M_{\text{star}}$  indicator, can be fitted well with the main stellar population alone (see Figure 3). We note that our main conclusions are unaffected, even if we miss some  $M_{\text{star}}$  contributed by the dust-enshrouded stellar population (see Section 3.1).

We note that another approach to account for the far-IR excess is to adopt a flat dust attenuation curve, which leads to significant attenuation at near-IR wavelengths (e.g., Buat et al. 2019). This method effectively assumes that the far-IR excess comes from the strong attenuation in the near-IR. We also test

<sup>19</sup> The Bayesian output is a probability-weighted value that considers all models available. It is thus more robust than the best-fit output, which is based on a single model with minimum  $\chi^2$ .

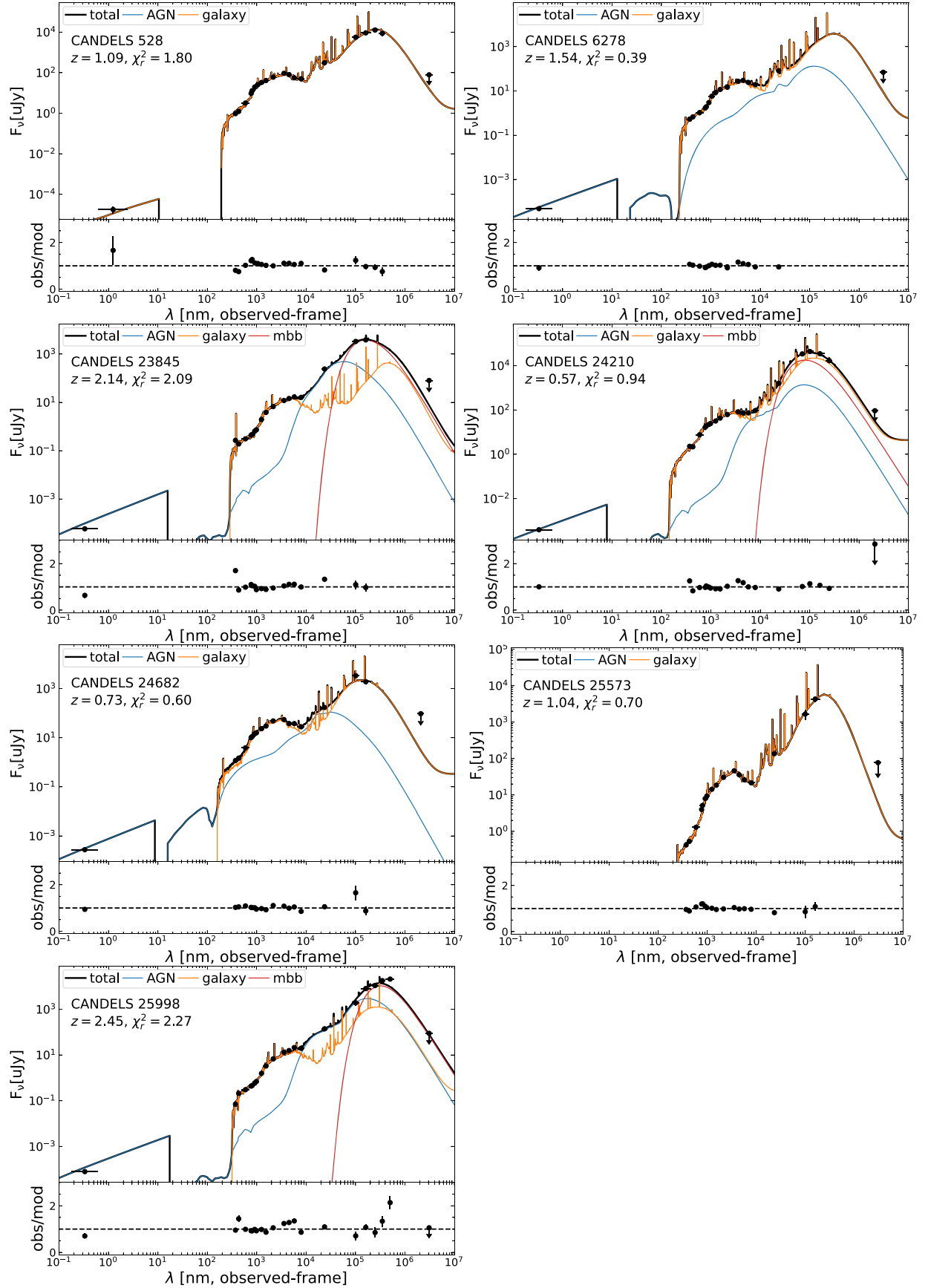


**Figure 3.** SED fits of our ALMA sources using CIGALE. The black curve represents the best-fit SED model, while the blue, orange, and red curves indicate AGN, galaxy, and mbb (if present) components, respectively. The redshift and reduced  $\chi^2$  are labeled on each panel.



this approach by allowing shallower interstellar medium (ISM) attenuation slopes ( $n_{\text{ISM}}$ ), ranging from  $-0.3$  to  $-0.7$  (disabling mbb). Indeed, the fit quality is improved (reduced  $\chi^2 \approx 2$ – $2.5$ ) compared to the original fits (reduced  $\chi^2 \approx 4$ – $5$ ). The resulting SFRs (also estimated from  $L_{\text{IR, gal}}$ ) are similar to those from the mbb fits, with differences  $\lesssim 0.1$  dex, but the  $M_{\text{star}}$  are systematically higher by  $\approx 0.3$ – $0.6$  dex.<sup>20</sup> These effects are similar to what Buat et al. (2019) found. In Section 3.1, we discuss the effects on our main conclusions if the flat curve approach is adopted instead of the mbb one.

The  $M_{\text{star}}$  and SFRs for all sources are listed in Table 1. Following Ni et al. (2021), we classify a source as a star-forming galaxy if it satisfies  $\text{SFR} > \text{SFR}_{\text{MS}}/10^{1.4}$ , where  $\text{SFR}_{\text{MS}}$  is the main-sequence SFR as a function of  $M_{\text{star}}$  and redshift from Whitaker et al. (2012). All seven of our sources are classified as SF galaxies. From Table 1, CANDELS 6278 has the largest SFR uncertainty (0.23 dex compared to  $\lesssim 0.05$  dex for the other sources).<sup>21</sup> This is understandable, as CANDELS 6278 is the only object without Herschel detections in our sample (see Figure 3). This level of SFR uncertainty (0.23 dex) without Herschel is realistic, based on previous studies with CIGALE (e.g., Mountrichas et al. 2021).

### 3. Discussion

#### 3.1. Implications for BH–Bulge Coevolution

With the measurements of galaxy properties in Section 2, we now discuss the implications for BH–bulge coevolution. First, we define a gas depletion timescale as

$$\tau_{\text{dep}} \equiv \frac{M_{\text{gas}}}{\text{SFR}}, \quad (4)$$

and a bulge stellar growth timescale as

$$\tau_{\text{grow}} \equiv \frac{M_{\text{star}}}{\text{SFR}}. \quad (5)$$

From this definition,  $\tau_{\text{grow}}$  represents the timescale needed to double the stellar mass in the future, given the current SFR. By denoting the galaxy’s redshift as corresponding to a universe age of  $t_0$ , and assuming that the SFR remains constant, with sufficient gas supply, the stellar mass at the cosmic time of  $t < t_0 + \tau_{\text{grow}}$  is dominantly assembled before  $t_0$ ; at  $t > t_0 + \tau_{\text{grow}}$ , the mass is dominantly assembled after  $t_0$ . This stellar growth timescale is also a proxy for the BH growth timescale, due to

$$\tau_{\text{grow}} = \frac{M_{\text{star}}}{\text{SFR}} = \frac{M_{\text{star}}/300}{\text{SFR}/300} \approx \frac{M_{\text{BH}}}{\text{BHAR}} = \tau_{\text{grow, BH}}, \quad (6)$$

where we apply the long-term average BHAR–SFR relation ( $\text{BHAR} \approx \text{SFR}/300$ ; see Section 1) and assume the local BH–bulge mass relation ( $M_{\text{BH}} \approx M_{\text{star}}/300$ ). We note that the system might not follow the local BH–bulge mass relation, and thus Equation (6) is only an approximation. If  $M_{\text{BH}}$  is higher (lower) than the local BH–bulge mass relation, then  $\tau_{\text{grow, BH}}$  should also be longer (shorter) than  $\tau_{\text{grow}}$ . The values of  $\tau_{\text{grow}}$

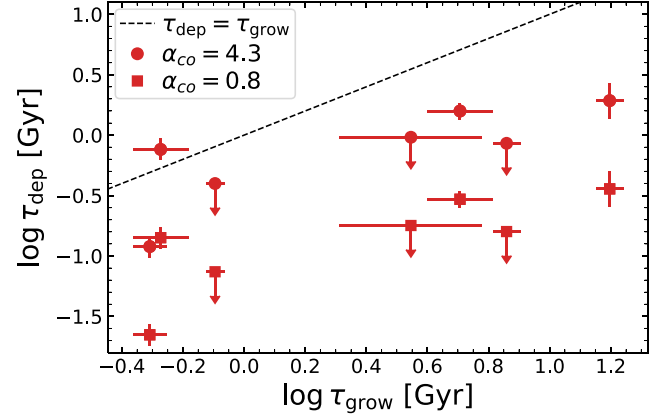


**Figure 4.**  $\tau_{\text{dep}}$  vs.  $\tau_{\text{grow}}$ . The red stars and squares are values estimated using  $\alpha_{\text{CO}} = 4.3$  (default) and  $\alpha_{\text{CO}} = 0.8$ , respectively. The downward-pointing arrows indicate  $3\sigma$  upper limits. The black dashed lines indicate  $\tau_{\text{dep}} = \tau_{\text{grow}}$ . Except for CANDELS 25998 ( $\alpha_{\text{CO}} = 4.3$ ), the other data points are all below the  $\tau_{\text{dep}} = \tau_{\text{grow}}$  line.

and  $\tau_{\text{dep}}$  for our targets are listed in Tables 1 and 2, respectively.

By comparing the two timescales of  $\tau_{\text{dep}}$  and  $\tau_{\text{grow}}$ , we can gain insight the BH–bulge coevolution. If  $\tau_{\text{dep}} > \tau_{\text{grow}}$ , then the gas content can last sufficiently long for significant BH/bulge growth, as the BH/bulge mass predominantly forms during the bulge phase, where the BHAR–SFR relation applies (Scenario 1 in Figure 1). Otherwise, the gas is depleted quickly, before significant BH/bulge growth, and the system cannot significantly change its position on the  $M_{\text{BH}}$ – $M_{\text{star}}$  diagram (Scenario 2 in Figure 1). Figure 4 compares  $\tau_{\text{dep}}$  versus  $\tau_{\text{grow}}$  for our ALMA targets. Six (of seven) SF sources have  $\tau_{\text{dep}} < \tau_{\text{grow}}$ , with the only exception being CANDELS 25998. For these six sources, their  $\tau_{\text{dep}}$  is more than two times shorter than  $\tau_{\text{grow}}$ .

Our estimates of  $M_{\text{gas}}$  assume a typical CO-to-gas conversion factor of  $\alpha_{\text{CO}} = 4.3$ . Some studies suggest a lower value of  $\alpha_{\text{CO}} = 0.8$  for compact galaxies (e.g., Bolatto et al. 2013; Carilli & Walter 2013). Considering that our bulge-dominated galaxies are generally compact (e.g., Ni et al. 2019, 2021), we also plot the result for the assumption of  $\alpha_{\text{CO}} = 0.8$  in Figure 4. Under this alternative assumption, all seven sources, including CANDELS 25998, have  $\tau_{\text{dep}}$  at least four times shorter than  $\tau_{\text{grow}}$ .

$\tau_{\text{dep}}$  and  $\tau_{\text{grow}}$  are measures of what can happen in the future life of the galaxy, assuming the current SFR. But the SFR is unlikely to remain constant over cosmic time. From hydrodynamical simulations, the SFR can be highly variable on relatively short timescales of  $\sim 10$  Myr (e.g., Flores Velázquez et al. 2021). However, from Equations (4) and (5), both  $\tau_{\text{dep}}$  and  $\tau_{\text{grow}}$  are inversely proportional to SFR, and thus their ratio is independent of SFR, i.e.,

$$\frac{\tau_{\text{dep}}}{\tau_{\text{grow}}} = \frac{M_{\text{gas}}}{M_{\text{star}}} \equiv \mu, \quad (7)$$

where  $\mu$  is also known as the gas fraction of the galaxy. To compare  $\tau_{\text{dep}}$  with  $\tau_{\text{grow}}$  is equivalent to comparing  $\mu$  with unity. The advantage of  $\mu$  is that it is not affected by the SFR variability mentioned above. Aside from this mathematical feature,  $\mu = M_{\text{gas}}/M_{\text{star}}$  also has a useful physical meaning: it represents the amount of mass that the BH/bulge can potentially grow in the future compared to the current mass.

<sup>20</sup> Based on these alternative estimations of SFRs and  $M_{\text{star}}$ , the sources are still classified as star-forming galaxies.

<sup>21</sup> The error is calculated by CIGALE as the standard deviation of the marginalized SFR probability distribution, accounting for all available physical models (Boquien et al. 2019).

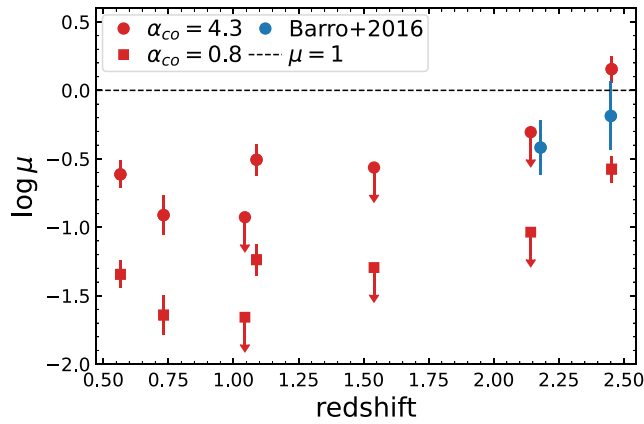


**Figure 5.**  $\mu = M_{\text{gas}}/M_{\text{star}}$  vs. redshift. The stars and squares are the values estimated using  $\alpha_{\text{CO}} = 4.3$  (default) and  $\alpha_{\text{CO}} = 0.8$ , respectively. The downward-pointing arrows indicate  $3\sigma$  upper limits. The dashed line indicates  $\mu = 1$ . The two blue data points represent two bulge-dominated galaxies at  $z = 2\text{--}2.5$  from Barro et al. (2016). The gas content of the bulge-dominated galaxies is generally low ( $\mu < 1$  in most cases), insufficient to support significant bulge/BH growth.

If  $\mu$  is above unity, the “potential” mass will be dominant, supporting Scenario 1 in Figure 1; otherwise, the “current” mass will be dominant, supporting Scenario 2 in Figure 1.

Figure 5 shows  $\mu$  versus redshift for our ALMA targets, under the assumptions of both  $\alpha_{\text{CO}} = 4.3$  and  $\alpha_{\text{CO}} = 0.8$ . As expected, all sources have  $\mu < 1$ , except CANDELS 25998 (for  $\alpha_{\text{CO}} = 4.3$ ). Considering the upper-limit data points, the median values of  $\mu$  are only  $< 0.26$  (for  $\alpha_{\text{CO}} = 4.3$ ) and  $< 0.048$  (for  $\alpha_{\text{CO}} = 0.8$ ), significantly smaller than unity under both  $\alpha_{\text{CO}}$  assumptions. The assumed CO line ratios are another source of systematic uncertainty. Our assumed values ( $r_{21} = 0.8$  and  $r_{31} = 0.5$ ) are typical among star-forming galaxies (e.g., Saintonge et al. 2017; Lamperti et al. 2020). Some observations suggest that AGN hosts (which is the case for many of our targets; Figure 3) tend to have  $r_{21}$  and  $r_{31}$  higher than normal galaxies (e.g., Kirkpatrick et al. 2019). We note that adopting higher  $r_{21}$  and  $r_{31}$  would decrease the final gas masses and  $\mu$ , and thereby strengthen our main result above.

In the discussion above, we assume that total  $M_{\text{star}} \approx$  bulge  $M_{\text{star}}$ , because our targets are bulge-dominated from HST imaging (Section 2.1). However, it is still possible that a minor disk component has been missed, which could account for  $< 40\%$  of the total mass (e.g., Huertas-Company et al. 2016). In the most extreme case (40% mass from a missed disk component), our bulge  $M_{\text{star}}$  is overestimated by a factor of  $1/(1 - 0.4) = 1.67$ , and thus  $\mu$  is underestimated by the same factor, according to Equation (7). Even this level of  $\mu$  underestimation is not strong enough to overturn our main result, as most sources (except CANDELS 25998, assuming  $\alpha_{\text{CO}} = 4.3$ ) will still have  $\mu < 1$  after correcting for the underestimation (see Table 2).

In Figure 5, we include two star-forming bulge-dominated sources that are also in the GOODS-South field from Barro et al. (2016).<sup>22</sup> One source is CANDELS 21662 at  $z = 2.18$ . The other is CANDELS 25998 at  $z = 2.45$ , which is also in our

sample. The Barro et al. (2016)  $M_{\text{gas}}$  values were from  $M_{\text{dust}}$ , assuming a gas-to-dust ratio of 100, and their  $M_{\text{dust}}$  estimation is based on SED modeling of ALMA continuum and other IR data. For CANDELS 25998, the Barro et al. (2016)  $M_{\text{gas}}$  ( $10^{10.9} M_{\odot}$ ) is consistent with our continuum-based  $M_{\text{gas}}$  constraint ( $< 10^{11.1} M_{\odot}$ ), although the two measurements are based on different frequencies and assumptions. The two  $\mu$  values from Barro et al. (2016) are both below unity, consistent with our sample. For CANDELS 25998, the Barro et al. (2016)  $M_{\text{star}}$  estimation is similar to ours ( $10^{11.07}$  versus  $10^{11.05} M_{\odot}$ ), and thus the cause of the  $\mu$  difference between Barro et al. (2016) and ours (the rightmost points in Figure 5) mostly relates to the  $M_{\text{gas}}$  measurements. The Barro et al. (2016)  $\mu$  is between our values, based on  $\alpha_{\text{CO}} = 0.8$  and  $\alpha_{\text{CO}} = 4.3$ , suggesting that the intrinsic  $\alpha_{\text{CO}}$  for this source is within 0.8–4.3. But we note that the uncertainties of the Barro et al. (2016)  $\mu$  are relatively large, and both our  $\mu$  values are consistent with their measurements at a  $2\sigma$  confidence level.

Our results above suggest that without gas replenishment (see Section 3.2), the cold molecular gas of the SF bulge-dominated galaxies will be depleted before significant BH/bulge growth. Their  $M_{\text{BH}}/M_{\text{star}}$  ratios remain largely unchanged during the bulge evolution phase until  $z = 0$  (see Section 1). Therefore, it is likely that the  $M_{\text{BH}}\text{--}M_{\text{star}}$  relation has already formed at the beginning of the bulge phase, and they maintain this relation until  $z = 0$  (i.e., Scenario 2 in Figure 1). The detailed formation mechanisms are unknown, being subject to investigations using both theoretical and observational approaches (e.g., Huertas-Company et al. 2018; Hopkins et al. 2022). The BHAR–bulge SFR relation has the role of maintaining the BH–bulge mass correlation, but not creating it. We caution that our sample is limited to  $z = 0.5\text{--}2.5$ . It is possible that this conclusion might change at higher redshifts, considering that cold gas tends to be more abundant toward the early universe. Also, from Figure 5, the  $z > 2$  sources tend to have higher  $\mu$  than sources at lower redshifts, although our sample size not sufficiently large to robustly test this trend.

In our SED fits (Section 2.5), we employ an ad hoc mbb component to account for the far-IR excess in three sources. We might underestimate  $M_{\text{star}}$  as we do not account for the mass contribution from the hidden stellar population. Therefore, the actual  $\mu$  values might be even lower than our case, further strengthening our main conclusion. The far-IR excess can also be addressed by adopting a flat attenuation curve. We note that this approach would also lead to higher  $M_{\text{star}}$  estimations (see Section 2.5), and thereby lower  $\mu$ . In summary, we consider that our main conclusion is not qualitatively affected by the details of the SED fitting procedure.

### 3.2. Gas Replenishment

The discussion in Section 3.1 assumes that the gas content in our bulge-dominated galaxies is primarily consumed by SF without replenishment. However, if gas replenishment is common, and supplies  $M_{\text{gas}}$  by a typical factor of  $\gtrsim 4$  (as the median  $\mu < 0.26$  for  $\alpha_{\text{CO}} = 4.3$  in Section 3.1), then the BH/bulge growth can be sustained for a longer timescale than our estimated  $\tau_{\text{dep}}$ .

This possibility can be qualitatively investigated by studying the fraction of star-forming galaxies, as common gas replenishment means widespread SF activity. Figure 6 displays the

<sup>22</sup> Barro et al. (2016) have six star-forming galaxies in total, but only two of them are bulge-dominated, according to the morphological classifications of Huertas-Company et al. (2015).

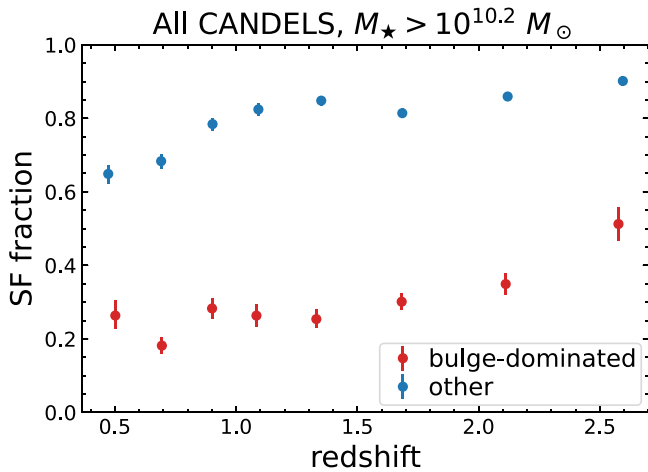


**Figure 6.** The fraction of star-forming galaxies ( $M_{\text{star}} > 10^{10.2} M_{\odot}$ ) as a function of redshift. The red data points represent bulge-dominated galaxies and the blue ones are for the other galaxies that are not bulge-dominated. The error bars represent  $1\sigma$  binomial uncertainties calculated with the “binom\_conf\_interval” function of ASTROPY. The star-forming fraction is low ( $\approx 0.2$ – $0.3$  at  $z \approx 0.5$ – $2$ ) for bulge-dominated galaxies, indicating that gas replenishment is not common for them.

SF fraction versus redshift among bulge-dominated galaxies in all five CANDELS fields. The sample’s properties (redshift,  $M_{\text{star}}$ , and SFR) are compiled/estimated by Yang et al. (2019). Here, we classify SF versus quiescent using the method in Section 2.5. The SF fraction values are calculated for galaxies more massive than  $10^{10.2} M_{\odot}$ , above which the bulge-dominated sample is complete up to  $z \approx 3$  (Yang et al. 2019).

From Figure 6, the SF fraction for bulge-dominated galaxies is generally low (e.g.,  $\approx 0.2$ – $0.3$  at  $z \approx 1$ – $2$ ). The low SF fraction suggests that bulge-dominated galaxies do not have prevalent strong gas replenishment, which is required to maintain their SF activity. In comparison, we also plot the SF fraction for galaxies that are not bulge-dominated (e.g., disk or irregular) in Figure 6. These galaxies tend to have high SF fractions (e.g.,  $\approx 0.8$ – $0.9$  at  $z \approx 1$ – $2$ ), indicating prevalent gas replenishment among them.

We caution that the argument above only qualitatively suggests that bulge-dominated galaxies have weaker gas replenishment than non-bulge-dominated galaxies. It does not rule out intermittent gas accretion among bulge-dominated galaxies. Intermittent gas accretion might lead to sporadic SF, which is also consistent with the low but nonzero SF fraction among bulge-dominated galaxies (see Figure 6). A quantitative assessment of intermittent gas accretion is beyond the scope of this work.

#### 4. Summary and Future Prospects

In this work, we have presented ALMA observations of seven bulge-dominated star-forming galaxies at  $z = 0.5$ – $2.5$ . Our main results are summarized below.

1. We have reduced the ALMA data and measured the CO(2–1) or CO(3–2) fluxes (see Section 2). We have detected the CO lines from four sources at  $>3\sigma$  levels, and we have estimated  $3\sigma$  upper limits for the other sources (Section 2.3). From these results, we have inferred molecular gas masses (or upper limits) assuming  $\alpha_{\text{CO}} = 4.3$ . By fitting the existing multiwavelength data

with CIGALE, we have estimated the stellar masses and SFRs for our ALMA targets (Section 2.5).

2. The gas depletion timescales are at least two times shorter than the corresponding bulge/BH growth timescales for most sources, except for CANDELS 25998 (see Section 3.1). The median value of  $\mu$  is only  $<0.26$ . If we assume  $\alpha_{\text{CO}} = 0.8$  (a typical value for compact galaxies) instead of  $\alpha_{\text{CO}} = 4.3$ , all sources have  $\mu < 0.25$  (i.e.,  $\tau_{\text{dep}}$  is  $>$  four times shorter than  $\tau_{\text{grow}}$ ), with a median  $<0.048$ . The ALMA continuum measurement from Barro et al. (2016) also suggest  $\mu < 1$  for two bulge-dominated sources (including CANDELS 25998). Therefore, we conclude that without strong gas replenishment (supplying  $M_{\text{gas}}$  by a factor of  $\gtrsim 4$ ), the observed gas content of the SF bulges is generally insufficient to support significant bulge/BH growth.
3. To assess the gas replenishment, we have estimated the SF fraction for a mass-complete sample of CANDELS galaxies (see Section 3.2). The SF fraction for bulge-dominated galaxies is much lower than that for non-bulge-dominated galaxies (e.g.,  $\approx 0.2$ – $0.3$  versus  $\approx 0.8$ – $0.9$  at  $z = 1$ – $2$ ). The low SF fraction of bulge-dominated galaxies indicates that gas replenishment is not a common process among them. We caution that our qualitative argument cannot rule out weak intermittent gas accretion among bulge-dominated galaxies.
4. Our overall results indicate that the  $M_{\text{BH}}$ – $M_{\text{star}}$  relation has already formed at the beginning of the bulge evolution phase (Scenario 2 in Figure 1). The systems then maintain this relation until  $z = 0$ . In other words, the BHAR–bulge SFR relation has the role of maintaining the BH–bulge mass correlation, but not creating it. Therefore, it will be useful to study BH–galaxy coevolution in the pre-bulge phase, which might reveal the mysterious origin of the  $M_{\text{BH}}$ – $M_{\text{star}}$  relation. Such a study would require reliable techniques, probably machine learning trained by hydrodynamical simulations (e.g., Huertas-Company et al. 2018), to select pre-bulge samples from high-resolution images.

Finally, we note that our sample size is limited (seven sources), and that they are all below  $z = 2.5$ . If this small sample is somehow biased toward the late stage of SF (Section 2.2), then our main conclusion could be altered. Future (sub)millimeter observations of a much larger ( $\gtrsim 100$ ) bulge-dominated sample over a wider parameter space (especially at  $z > 2.5$ ) will naturally address this potential issue, and further test our conclusion. High-redshift morphological classifications, which are necessary for selecting bulge-dominated sources, will be available in the near future, with the advance of JWST extragalactic surveys. ALMA or other (sub) millimeter facilities can perform follow-up observations of the JWST-selected targets.

We thank the referee for helpful feedback that improved this work. We thank Guillermo Barro and Ian Smail for helpful discussions. G.Y., C.P., J.S.S., J.L.W., and C.P.Z. acknowledge support from the George P. and Cynthia Woods Mitchell Institute for Fundamental Physics and Astronomy at Texas A&M University. W.N.B. acknowledges support from Chandra X-ray Center grant GO9-20099X and the V.M. Willaman Endowment. D.M.A. thanks the Science and Technology Facilities Council for support through grant

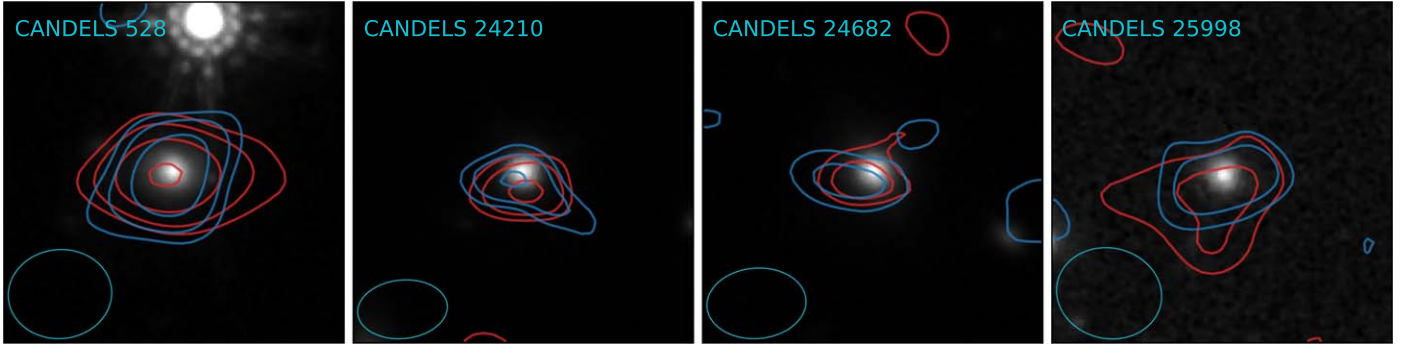
code ST/T000244/1. M.B. gratefully acknowledges support from the ANID BASAL project FB210003 and from the FONDECYT regular grant 1211000. The authors acknowledge the Texas A&M University Brazos HPC cluster and Texas A&M High Performance Research Computing Resources (HPRC; <http://hprc.tamu.edu>), which contributed to the research reported here. We thank the ALMA helpdesk for their help with ALMA data retrieval and reduction. This paper makes use of the following ALMA data: ADS/JAO.ALMA#2019.1.00678.S. The Joint ALMA Observatory is operated by ESO, AUI/NRAO, and NAOJ. The National Radio Astronomy Observatory is a facility of the National Science Foundation, operated under cooperative agreement by Associated Universities, Inc. This work has made use of the Rainbow Cosmological Surveys Database, which is operated by the Centro de Astrobiología (CAB/INTA), partnered with the University of California Observatories at Santa Cruz (UCO/Lick, UCSC).

*Software:* ASTROPY (v4.2; Astropy Collaboration et al. 2018), CIGALE (v2022.0; Boquien et al. 2019; Yang et al. 2020, 2022), CASA (v6.2.0; McMullin et al. 2007).

## Appendix Spatial Analysis

For the four CO-detected sources (Section 2.3), we further perform spatial analysis for their lines. For each of the four sources, we divide the line into blue and red halves, and make a line image for each half. The resulting line image contours are displayed in Figure 7. From this figure, only CANDELS 24210 appears to have (slightly) separated blue versus red contours. The angular distance between the blue and red peaks is  $\approx 0''.5$ . On the other hand, the positional uncertainty of the blue/red line emission is  $\approx 0.6\theta(S/N)^{-1} \approx 0''.26$ , where  $\theta \approx 1''.5$  is the synthesized beam FWHM (e.g., Ivison et al. 2007). Therefore, the  $\approx 0''.5$  separation is marginally significant at a  $\approx 2\sigma$  level.







The results above indicate that our current ALMA data are not able to spatially resolve the line-emitting regions in general. This is understandable, considering the relatively large beam sizes compared to the *H*-band profiles (see Figure 7). High-resolution ALMA runs will be necessary to probe the spatial distribution of the CO emission.



**Figure 7.** HST *H*-band  $7'' \times 7''$  cutouts with contours of CO emission, for the four CO-detected sources. The blue and red contours are from the blue and red halves of the line, respectively. The contours are at the  $2\sigma$ ,  $3\sigma$ ,  $5\sigma$ , and  $8\sigma$  levels. The beam profile is displayed in the bottom left corner.



## ORCID iDs

Guang Yang (杨光)  <https://orcid.org/0000-0001-8835-7722>  
 David M. Alexander  <https://orcid.org/0000-0002-5896-6313>  
 Médéric Boquien  <https://orcid.org/0000-0003-0946-6176>  
 Casey Papovich  <https://orcid.org/0000-0001-7503-8482>  
 Justin S. Spilker  <https://orcid.org/0000-0003-3256-5615>  
 Fabio Vito  <https://orcid.org/0000-0003-0680-9305>  
 Jonelle L. Walsh  <https://orcid.org/0000-0002-1881-5908>

## References

- Aird, J., Coil, A. L., & Georgakakis, A. 2018, *MNRAS*, **474**, 1225  
 Akaike, H. 1974, *ITAC*, **19**, 716  
 Astropy Collaboration, Price-Whelan, A. M., Sipőcz, B. M., et al. 2018, *AJ*, **156**, 123  
 Barro, G., Faber, S. M., Perez-Gonzalez, P. G., et al. 2013, *ApJ*, **765**, 104  
 Barro, G., Kriek, M., Perez-Gonzalez, P. G., et al. 2016, *ApJL*, **827**, L32  
 Barro, G., Perez-Gonzalez, P. G., Cava, A., et al. 2019, *ApJS*, **243**, 22  
 Bolatto, A. D., Wolfire, M., & Leroy, A. K. 2013, *ARA&A*, **51**, 207  
 Boquien, M., Burgarella, D., Roehlly, Y., et al. 2019, *A&A*, **622**, A103  
 Brandt, W. N., & Yang, G. 2021, arXiv:2111.01156  
 Bruzual, G., & Charlot, S. 2003, *MNRAS*, **344**, 1000  
 Buat, V., Ciesla, L., Boquien, M., Malek, K., & Burgarella, D. 2019, *A&A*, **632**, A79  
 Burnham, K., & Anderson, D. 2002, Model selection and multimodel inference: a practical information-theoretic approach, Vol. 2 (Berlin: Springer), 49  
 Carilli, C. L., & Walter, F. 2013, *ARA&A*, **51**, 105  
 Chabrier, G. 2003, *ApJL*, **586**, L133  
 Charlot, S., & Fall, S. M. 2000, *ApJ*, **539**, 718  
 Coil, A. L., Aird, J., Reddy, N., et al. 2015, *ApJ*, **801**, 35  
 Conselice, C. J. 2014, *ARA&A*, **52**, 291  
 Cooper, M. C., Yan, R., Dickinson, M., et al. 2012, *MNRAS*, **425**, 2116  
 Dale, D. A., Helou, G., Magdis, G. E., et al. 2014, *ApJ*, **784**, 83  
 Elbaz, D., Dickinson, M., Hwang, H. S., et al. 2011, *A&A*, **533**, A119  
 Estrada-Carpenter, V., Papovich, C., Momcheva, I., et al. 2020, *ApJ*, **898**, 171  
 Flores Velázquez, J. A., Gurvich, A. B., Faucher-Giguere, C.-A., et al. 2021, *MNRAS*, **501**, 4812  
 Freundlich, J., Combes, F., Tacconi, L. J., et al. 2019, *A&A*, **622**, A105  
 Georgakakis, A., Aird, J., Schulze, A., et al. 2017, *MNRAS*, **471**, 1976  
 Greene, J. E., Strader, J., & Ho, L. C. 2020, *ARA&A*, **58**, 257  
 Grogin, N. A., Kocevski, D. D., Faber, S. M., et al. 2011, *ApJS*, **197**, 35  
 Guo, Y., Ferguson, H. C., Gialvalisco, M., et al. 2013, *ApJS*, **207**, 24  
 Harrison, C. M. 2017, *NatAs*, **1**, 0165  
 Hickox, R. C., Mullaney, J. R., Alexander, D. M., et al. 2014, *ApJ*, **782**, 9  
 Hodge, J. A., Swinbank, A. M., Simpson, J. M., et al. 2016, *ApJ*, **833**, 103  
 Hopkins, P. F., Wellons, S., Angles-Alcazar, D., Faucher-Giguere, C.-A., & Grudic, M. Y. 2022, *MNRAS*, **510**, 630  
 Huertas-Company, M., Bernardi, M., Perez-Gonzalez, P. G., et al. 2016, *MNRAS*, **462**, 4495  
 Huertas-Company, M., Gravet, R., Cabrera-Vives, G., et al. 2015, *ApJS*, **221**, 8  
 Huertas-Company, M., Primack, J. R., Dekel, A., et al. 2018, *ApJ*, **858**, 114  
 Ivison, R. J., Greve, T. R., Dunlop, J. S., et al. 2007, *MNRAS*, **380**, 199  
 Jahnke, K., & Macció, A. V. 2011, *ApJ*, **734**, 92  
 Kennicutt, R. C., Jr. 1998, *ApJ*, **498**, 541  
 King, A., & Pounds, K. 2015, *ARA&A*, **53**, 115  
 Kirkpatrick, A., Sharon, C., Keller, E., & Pope, A. 2019, *ApJ*, **879**, 41  
 Kocevski, D. D., Barro, G., Faber, S. M., et al. 2017, *ApJ*, **846**, 112  
 Koekemoer, A. M., Faber, S. M., Ferguson, H. C., et al. 2011, *ApJS*, **197**, 36  
 Kormendy, J., & Ho, L. C. 2013, *ARA&A*, **51**, 511  
 Lamperti, I., Saintonge, A., Koss, M., et al. 2020, *ApJ*, **889**, 103  
 Luo, B., Brandt, W. N., Xue, Y. Q., et al. 2017, *ApJS*, **228**, 2  
 Lutz, D., Poglitsch, A., Altieri, B., et al. 2011, *A&A*, **532**, A90  
 McMullin, J. P., Waters, B., Schiebel, D., Young, W., & Golap, K. 2007, in ASP Conf. Ser., 376, Astronomical Data Analysis Software and Systems XVI, ed. R. A. Shaw, F. Hill, & D. J. Bell (San Francisco, CA: ASP), 127  
 Mountrichas, G., Buat, V., Yang, G., et al. 2021, *A&A*, **653**, A74  
 Ni, Q., Brandt, W. N., Yang, G., et al. 2021, *MNRAS*, **500**, 4989  
 Ni, Q., Yang, G., Brandt, W. N., et al. 2019, *MNRAS*, **490**, 1135  
 Papovich, C., Dickinson, M., Gialvalisco, M., Conselice, C. J., & Ferguson, H. C. 2005, *ApJ*, **631**, 101  
 Peng, C. Y. 2007, *ApJ*, **671**, 1098  
 Ramos Padilla, A. F., Wang, L., Malek, K. n., Efstathiou, A., & Yang, G. 2022, *MNRAS*, **510**, 687  
 Roehlly, Y., Burgarella, D., Buat, V., et al. 2014, in ASP Conf. Ser., 485, Astronomical Data Analysis Software and Systems XXIII, ed. N. Manset & P. Forshay (San Francisco, CA: ASP), 347  
 Saglia, R. P., Opitsch, M., Erwin, P., et al. 2016, *ApJ*, **818**, 47  
 Saintonge, A., Catinella, B., Tacconi, L. J., et al. 2017, *ApJS*, **233**, 22  
 Salim, S., Rich, R. M., Charlot, S., et al. 2007, *ApJS*, **173**, 267  
 Scoville, N., Sheth, K., Aussel, H., et al. 2016, *ApJ*, **820**, 83  
 Scoville, N., Lee, N., Bout, P. V., et al. 2017, *ApJ*, **837**, 150  
 Shanguan, J., Ho, L. C., Bauer, F. E., Wang, R., & Treister, E. 2020, *ApJ*, **899**, 112  
 Solomon, P. M., & Vanden Bout, P. A. 2005, *ARA&A*, **43**, 677  
 Stalevski, M., Fritz, J., Baes, M., Nakos, T., & Popović, L. Č. 2012, *MNRAS*, **420**, 2756  
 Stalevski, M., Ricci, C., Ueda, Y., et al. 2016, *MNRAS*, **458**, 2288  
 Suh, H., Hasinger, G., Steinhardt, C., Silverman, J. D., & Schramm, M. 2015, *ApJ*, **815**, 129  
 Vanzella, E., Cristiani, S., Dickinson, M., et al. 2008, *A&A*, **478**, 83  
 Whitaker, K. E., van Dokkum, P. G., Brammer, G., & Franx, M. 2012, *ApJL*, **754**, L29  
 Yang, G., Brandt, W. N., Alexander, D. M., et al. 2019, *MNRAS*, **485**, 3721  
 Yang, G., Brandt, W. N., Vito, F., et al. 2018, *MNRAS*, **475**, 1887  
 Yang, G., Boquien, M., Brandt, W. N., et al. 2022, *ApJ*, **927**, 192  
 Yang, G., Boquien, M., Buat, V., et al. 2020, *MNRAS*, **491**, 740  
 Yang, G., Chen, C.-T.-J., Vito, F., et al. 2017, *ApJ*, **842**, 72  
 Yang, G., Estrada-Carpenter, V., Papovich, C., et al. 2021, *ApJ*, **921**, 170